이학석사 학위논문

Dynamic force microscopy
using multi-harmonic signal analysis

다중 조파 신호 분석을 이용한 동역학 힘 현미경법

2021년 2월

서울대학교 대학원

물리·천문학부

김 성 훈

Dynamic force microscopy
using multi-harmonic signal analysis

다중 조파 신호 분석을 이용한 동역학 힘 현미경법

指導教授 諸元鎬

이 論文을 理學碩士學位論文으로 提出함

2020年　11月

서울大學校 大學院

物理·天文學部

金 成 訓

金成訓의 理學碩士 學位論文을 認准함

2020年　12月

委 員 長　　홍 승 훈
副委員長　　제 원 호
委 員　　박 철 환

Dynamic force microscopy
using multi-harmonic signal analysis

by

Sunghoon Kim, B.S.

Thesis

Presented to the Faculty of the Graduate School of

Seoul National University

in Partial Fulfillment

of the Requirements

for the Degree of

Master of Science

Seoul National University

February 2021

Abstract

Dynamic force microscopy using multi-harmonic signal analysis

Sunghoon Kim
Department of Physics and Astronomy
The Graduate School
Seoul National University

The success of the dynamic force microscopy (DFM) in quantifying structures and features of material surfaces at the atomic and molecular level has led to numerous progress in condensed matter physics, chemistry, biology, and material science. Its success is based on the ability to measure the local physical forces between the DFM probe and sample with spatial resolution ranging from few micrometers to sub-nanometers. Measuring forces using DFM requires conversion of the perturbed motion of the probe due to tip-sample interactions to force-distance curves, which is called force reconstruction. However, the most widely used force reconstruction method has recently been reported to yield non-negligible error and exhibit reconstruction instabilities when the oscillation amplitude is comparable to the decay length of the interaction. The main reason for these failures at such amplitudes is that the probe oscillation is no longer simply harmonic, which conventional methods assume, as higher harmonic motions become considerable at the regime where force changes rapidly. Consequently,

a novel, universal force reconstruction scheme that works in all amplitudes and the entire tip-sample distances has become crucial.

This thesis resolves this issue by developing DFM based on multi-harmonic signal analysis. This platform enables versatile force reconstruction using signals not only at the resonance frequency of the DFM probe, but also at its higher harmonics. Here, the following studies are performed for formulation of this new approach. First, the higher harmonic signals in DFM are theoretically analyzed. Exact, analytic expressions for higher harmonics generated from arbitrary conservative and dissipative forces are derived for two operation modes of DFM, amplitude-modulation and frequency-modulation. Moreover, universal force reconstruction formulas, which completely recover both the conservative and dissipative forces for entire oscillation amplitudes and tip-sample distances, are derived for two operation modes of DFM. This approach provides force reconstruction scheme that outperforms the conventional methods in two ways: (i) the higher accuracy at faster computation speed even by employing an approximated form of the reconstruction formulas, and (ii) the greater robustness with respect to the oscillation-amplitude error, overcoming the reconstruction instability. This thesis is expected to be of great potential importance in the field of surface science, as it may lead to a significant improvement in DFM-based experiments, including single molecule detection, identification of physicochemical interactions, and discovery of novel electron transport properties.

Multi-harmonic Atomic Force Microscopy, Spectral Analysis, Harmonic

Analysis, Non-linear Dynamics

Student number :   2019-22272

Contents

List of Figures

Chapter 1

Introduction

1.1 Dynamic Force Microscopy

Dynamic force microscopy (DFM) is one of the most precise type of scanning probe microscopy that opened the doors to the atomic and molecular world. The invention of the scanning tunneling microscope (STM) by Binnig *et al.* [1] thirty-nine years ago was succeeded by the advent of atomic force microscopy (AFM) five years later [2]. Within nine years of its arrival, the dynamic mode AFM, also known as DFM, has demonstrated the atomic resolution imaging of silicon (111)-(7×7) surface [3]. DFM was further utilized to probe and manipulate objects at an atomic level, enabling applications to various fields including condensed matter physics [4–6], chemistry [7], biology [8,9], and material science [10].

The principle of AFM operation is based on the interaction between a sharp tip of the AFM probe and a sample, which causes perturbation of the

probe from its initial state [11]. The AFM probe is typically composed of a cantilever and a sharp tip attached at its end. In static mode AFM, which is the most basic operation mode of AFM, the probe interacts with the surface atoms, and commensurate deflections of the cantilever occur, which are detected using a laser beam reflected from the cantilever. Static mode AFM is widely used in structural imaging, where the probe is moved physically closer to or further away from the surface to maintain a constant deflection, while it scans the sample surface. Another important application of static mode AFM is force spectroscopy, where the deflection is monitored at a single point of the sample as the probe moves vertically to or away from the sample. However, a critical problem in AFM is jump-to-contact, where its tip is made in contact with the surface when the attractive force exceeds the restoring force of the cantilever. Such behavior reduces measurement accuracy and causes mechanical damages to the sample. While the use of stiff cantilevers can resolve this issue, it poses a different problem: signal-to-noise ratio (SNR) decreases since stiffer cantilevers deflect less to tip-sample interaction force. In DFM, the cantilever is driven externally as it interacts with the sample [12] to achieve the greater SNR and enhanced sensitivity to short-range forces. There are two operation schemes of DFM; in frequency-modulation AFM (FM-AFM), the oscillation frequency of the cantilever matches its resonance, whereas in amplitude-modulation AFM (AM-AFM), the probe oscillates at a fixed frequency. In contrast to force spectroscopy using static mode AFM, where the force can be directly converted from the deflection of the probe, that in DFM is not so straightforward since DFM

2

measures the perturbed dynamic motion of the probe due the force acted on the probe during its oscillations. Hence, an additional procedure is required to convert experimental data to force-distance curves, which is called force reconstruction.

1.2   Force Reconstruction in Dynamic Force Microscopy

Force reconstruction in DFM is a nontrivial problem since it requires deconvolution of the tip oscillation to recover tip-sample interaction. Several proposed methods include the use of iterative calculations [13, 14], matrix inversions [15], infinite summations of higher order derivatives [16] and Chebyshev polynomials [17]. Such methods are of limited practicality and/or under-performance because heavy calculations are required to achieve desired accuracy [18, 19]. A practical method most widely used in both FM-AFM [20] and AM-AFM [18, 21] operations is the integration method of Sader and Jarvis [20], called the Sader-Jarvis (SJ) method, as it provides good approximation to the underlying forces using simple integrals.

Nonetheless, however, recent reports suggested non-negligible error and exhibit reconstruction instability of the SJ method when the oscillation amplitude is comparable to the decay length λ of the interaction forces [18, 20, 22–24]. Using amplitudes smaller or larger than λ can bypass this issue, despite the requirement of additional experimental procedures to identify (possibly multi-

ple) λ's [24, 25], which are generally not known *a priori*. However, this bypass strategy has a trade-off: since it sacrifices both the SNR [26] and the sensitivity to the short-range forces [11], one requires not only costly instruments and long data acquisition times to achieve low noise, but also excessive experimental procedures to isolate the short-range contributions from the measured forces. Indeed, to optimize signal measurement, amplitudes comparable to λ have been used in DFM experiments, particularly in recent researches in condensed-matter physics [5, 27–30]. Nonetheless, choosing such amplitudes in conventional force-reconstruction procedures may lead to failure to accurately recover the fine details of the force. Such failure is due to the discrepancy between the assumption used in the reconstruction formulas (i.e., single-frequency cantilever motion at resonance) and the actual cantilever dynamics which can become significantly anharmonic, especially in the rapidly changing regime of the force. Therefore, an accurate and robust force reconstruction platform for DFM, valid in the entire range of amplitudes is yet conceived.

1.3   Multi-harmonic Atomic Force Microscopy

In multi-harmonic AFM (MHAFM), the anharmonic motion of the cantilever is considered to enhance the capability of the conventional AFM. MHAFM additionally detects the higher harmonic signals during AM-AFM or FM-AFM operations to attain greater spatial resolutions [31–34] and characterize the local properties in more detail [35–38]. Detection bandwidth and resolution of

multi-harmonic signals have been further advanced by the use of novel signal processing filters [39, 40] and signal enhancement effects of the resonant harmonics of cantilevers [41, 42] as well as piezoelectric effects of quartz tuning forks [33, 34].

While understanding higher harmonic motions in DFM is crucial to address the 'pothole' in conventional force reconstructions, theoretical formulations of MHAFM remain incomplete; existing analytical expressions for higher harmonic signals of arbitrary harmonic order are derived only for high-vacuum FM-AFM operations [43], which still requires a general framework for both MHAFM modes to resolve the 'pothole'.

1.4   Outline of the Thesis

This thesis formulates a new platform of DFM using multi-harmonic signal analysis through following chapters. In Chapter 2, higher harmonic signals in DFM is studied based on rigorous theoretical formulations. The DFM probe is modeled as a driven harmonic oscillator induced by tip-sample interactions. Using typical assumptions made in DFM studies, highly accurate and analytic expressions for higher harmonics in DFM is derived for both types of DFM and for arbitrary conservative and dissipative forces. Then, Chapter 3 builds upon the theoretical studies of the higher harmonics by providing inversion formulas for force reconstruction. Laplace transformations, followed by analytic calculations are performed to derive reconstruction formulas from multi-harmonic signals.

Reconstruction of simulated force curves from generated multi-harmonic signals in both AM-AFM and FM-AFM demonstrates high accuracy and robustness of multi-harmonic signal analysis-based DFM. Chapter 4 concludes this thesis by providing a short summary of the major contributions and discussions and leaving comments about prospective impacts on condensed matter physics.

Bibliography

[1] Binnig, G., Rohrer, H., Gerber, C. & Weibel, E. Tunneling through a controllable vacuum gap. *Appl. Phys. Lett.* **40**, 178–180 (1982).

[2] Binnig, G., Quate, C. F. & Gerber, C. Atomic force microscope. *Phys. Rev. Lett.* **56**, 930–933 (1986).

[3] Giessibl, F. J. Atomic-resolution of the silicon (111)-(7x7) surface by atomic-force microscopy. *Science* **267**, 68–71 (1995).

[4] Ternes, M., Lutz, C. P., Hirjibehedin, C. F., Giessibl, F. J. & Heinrich, A. J. The force needed to move an atom on a surface. *Science* **319**, 1066–1069 (2008).

[5] Pielmeier, F. & Giessibl, F. J. Spin resolution and evidence for superexchange on nio(001) observed by force microscopy. *Phys. Rev. Lett.* **110**, 266101 (2013).

[6] Kawai, S. *et al.* Superlubricity of graphene nanoribbons on gold surfaces. *Science* **351**, 957–61 (2016).

[7] Sugimoto, Y. *et al.* Chemical identification of individual surface atoms by atomic force microscopy. *Nature* **446**, 64–67 (2007).

[8] Anselmetti, D. *et al.* Attractive-mode imaging of biological materials with dynamic force microscopy. *Nanotechnology* **5**, 87–94 (1994).

[9] Bustamante, C. & Keller, D. Scanning force microscopy in biology. *Phys. Today* **48**, 32–38 (1995).

[10] Garcıa, R., Calleja, M. & Pérez-Murano, F. Local oxidation of silicon surfaces by dynamic force microscopy: Nanofabrication and water bridge formation. *Appl. Phys. Lett.* **72**, 2295–2297 (1998).

[11] Giessibl, F. J. Advances in atomic force microscopy. *Rev. Mod. Phys.* **75**, 949–983 (2003).

[12] Garcia, R. & Pérez, R. Dynamic atomic force microscopy methods. *Surf. Sci. Rep.* **47**, 197–301 (2002).

[13] Dürig, U. Extracting interaction forces and complementary observables in dynamic probe microscopy. *Appl. Phys. Lett.* **76**, 1203–1205 (2000).

[14] Gotsmann, B., Seidel, C., Anczykowski, B. & Fuchs, H. Conservative and dissipative tip-sample interaction forces probed with dynamic afm. *Phys. Rev. B* **60**, 11051–11061 (1999).

[15] Giessibl, F. J. A direct method to calculate tip–sample forces from fre-

quency shifts in frequency-modulation atomic force microscopy. *Appl. Phys. Lett.* **78**, 123–125 (2001).

[16] Lee, M. & Jhe, W. General theory of amplitude-modulation atomic force microscopy. *Phys. Rev. Lett.* **97**, 036104 (2006).

[17] Hu, S. & Raman, A. Inverting amplitude and phase to reconstruct tip-sample interaction forces in tapping mode atomic force microscopy. *Nanotechnology* **19**, 375704 (2008).

[18] Dagdeviren, O. E., Zhou, C., Altman, E. I. & Schwarz, U. D. Quantifying tip-sample interactions in vacuum using cantilever-based sensors: An analysis. *Phys. Rev. Appl.* **9**, 044040 (2018).

[19] Welker, J., Illek, E. & Giessibl, F. J. Analysis of force-deconvolution methods in frequency-modulation atomic force microscopy. *Beilstein J. Nanotechnol.* **3**, 238–48 (2012).

[20] Sader, J. E. & Jarvis, S. P. Accurate formulas for interaction force and energy in frequency modulation force spectroscopy. *Appl. Phys. Lett.* **84**, 1801–1803 (2004).

[21] Payam, A. F., Martin-Jimenez, D. & Garcia, R. Force reconstruction from tapping mode force microscopy experiments. *Nanotechnology* **26**, 185706 (2015).

[22] Katan, A. J., van Es, M. H. & Oosterkamp, T. H. Quantitative force

versus distance measurements in amplitude modulation afm: a novel force inversion technique. *Nanotechnology* **20**, 165703 (2009).

[23] Dagdeviren, O. E. & Schwarz, U. D. Accuracy of tip-sample interaction measurements using dynamic atomic force microscopy techniques: Dependence on oscillation amplitude, interaction strength, and tip-sample distance. *Rev. Sci. Instrum.* **90**, 033707 (2019).

[24] Sader, J. E., Hughes, B. D., Huber, F. & Giessibl, F. J. Interatomic force laws that evade dynamic measurement. *Nat. Nanotechnol.* **13**, 1088–1091 (2018).

[25] Huber, F. & Giessibl, F. J. Experimental use of the inflection point test for force deconvolution in frequency-modulation atomic force microscopy to turn an ill-posed situation into a well-posed one by proper choice of amplitude. *J. Appl. Phys.* **127**, 184301 (2020).

[26] Giessibl, F. J., Bielefeldt, H., Hembacher, S. & Mannhart, J. Calculation of the optimal imaging parameters for frequency modulation atomic force microscopy. *Appl. Surf. Sci.* **140**, 352–357 (1999).

[27] Gross, L., Mohn, F., Moll, N., Liljeroth, P. & Meyer, G. The chemical structure of a molecule resolved by atomic force microscopy. *Science* **325**, 1110–1114 (2009).

[28] Pavliček, N. & Gross, L. Generation, manipulation and characterization of molecules by atomic force microscopy. *Nat. Rev. Chem.* **1**, 0005 (2017).

[29] Huber, F. *et al.* Chemical bond formation showing a transition from physisorption to chemisorption. *Science* **366**, 235–238 (2019).

[30] Berwanger, J., Polesya, S., Mankovsky, S., Ebert, H. & Giessibl, F. J. Atomically resolved chemical reactivity of small fe clusters. *Phys. Rev. Lett.* **124**, 096001 (2020).

[31] Crittenden, S., Raman, A. & Reifenberger, R. Probing attractive forces at the nanoscale using higher-harmonic dynamic force microscopy. *Phys. Rev. B* **72**, 235422 (2005).

[32] Stark, R. W. & Heckl, W. M. Higher harmonics imaging in tapping-mode atomic-force microscopy. *Rev. Sci. Instrum.* **74**, 5111–5114 (2003).

[33] Giessibl, F. J. Higher-harmonic atomic force microscopy. *Surf. Interface Anal.* **38**, 1696–1701 (2006).

[34] Hembacher, S., Giessibl, F. J. & Mannhart, J. Force microscopy with light-atom probes. *Science* **305**, 380–383 (2004).

[35] Gramazio, F. *et al.* Functional dependence of resonant harmonics on nanomechanical parameters in dynamic mode atomic force microscopy. *Beilstein J. Nanotechnol.* **8**, 883–891 (2017).

[36] Gramazio, F., Lorenzoni, M., Perez-Murano, F., Evangelio, L. & Fraxedas, J. Quantification of nanomechanical properties of surfaces by higher har-

monic monitoring in amplitude modulated afm imaging. *Ultramicroscopy* **187**, 20–25 (2018).

[37] Shaik, N. H., Reifenberger, R. G. & Raman, A. Nanomechanical mapping in air or vacuum using multi-harmonic signals in tapping mode atomic force microscopy. *Nanotechnology* **31**, 455502 (2020).

[38] Raman, A. *et al.* Mapping nanomechanical properties of live cells using multi-harmonic atomic force microscopy. *Nat. Nanotechnol.* **6**, 809–814 (2011).

[39] Ruppert, M. G., Harcombe, D. M. & Moheimani, S. O. R. High-bandwidth demodulation in mf-afm: A kalman filtering approach. *IEEE/ASME Trans. Mechatron.* **21**, 2705–2715 (2016).

[40] Harcombe, D. M., Ruppert, M. G., Ragazzon, M. R. P. & Fleming, A. J. Lyapunov estimation for high-speed demodulation in multifrequency atomic force microscopy. *Beilstein J. Nanotechnol.* **9**, 490–498 (2018).

[41] Sahin, O. & Atalar, A. Simulation of higher harmonics generation in tapping-mode atomic force microscopy. *Appl. Phys. Lett.* **79**, 4455–4457 (2001).

[42] Sahin, O., Quate, C. F., Solgaard, O. & Atalar, A. Resonant harmonic response in tapping-mode atomic force microscopy. *Phys. Rev. B* **69**, 165416 (2004).

[43] Dürig, U. Interaction sensing in dynamic force microscopy. *New J. Phys.* **2**, 5–5 (2000).

Chapter 2

Generation of Higher Harmonics in Dynamic Force Microscopy

2.1 Introduction

Higher harmonic responses of physical systems provide rich information of the physical characteristics of the underlying structures pertaining to the driving force. While the potential energy of the physical system is approximately harmonic near its equilibrium state, most systems become anharmonic for large perturbations, which gives rise to higher harmonic behaviors. In conducting materials, electrons are excited using a laser, where the higher harmonic response of the electrons is used to characterize the electron-nucleus interactions [1–3]. Similarly, in dynamic force microscopy (DFM), the external driving forces the DFM cantilever probe to oscillate, and high harmonics of the cantilever motion

are generated due to anaharmonic tip-sample interactions.

This chapter describes derivation of exact, analytic expressions for the higher harmonics of the DFM cantilever motion in both AM-AFM and FM-AFM. The physical meanings of higher harmonic signals are discussed. Also, simulation results of multi-harmonic signals assuming Lennard-Jones type force as the tip-sample interaction is shown. This chapter provides general theoretical formulations for rigorous analysis in MHAFM.

2.2   Theoretical Formulation

The motion of the cantilever probe is typically modeled as a harmonic oscillator with external driving force and interaction force [4, 5],

$$m\ddot{\xi} + b\dot{\xi} + k\xi = kA_d \cos \omega t + F_{\text{int}}, \tag{2.1}$$

where ξ is the displacement of the probe, m the effective mass, b the damping coefficient, and k the stiffness of the probe. The coefficients on the left-hand side of the equation are related to the unperturbed resonance frequency ω_0 and the quality factor Q, where $b = m\omega_0/Q$ and $k = m\omega_0^2$. The right-hand side of the equation represents the tip-sample interaction force F_{int} and the external driving force with driving amplitude A_d and frequency ω. As the cantilever graudally approaches the surface, the nonlinearity of F_{int} within the oscillation range generates multi-harmonic motion of the probe. Thus, ξ can be described

in terms of the relative distance z between the tip and substrate atoms;

$$\xi(z, t) = \xi_0(z) + \sum_{n=1}^{\infty} A_n(z) \sin(n\omega t + \theta_n(z)), \tag{2.2}$$

where $A_n(z)$ and $\theta_n(z)$ denote the amplitude and phase, respectively, of the nth harmonic motion and $\xi_0(z)$ is the mean deflection of the probe.

The interaction force can be decomposed into the conservative and dissipative (non-conservative) terms,

$$F_{\text{int}}(z, \dot{z}) = F_c(z) + F_{\text{nc}}(z, \dot{z}). \tag{2.3}$$

Combining Eqs. (2.1) and (2.3), we obtain the dissipation energy of the probe for a single oscillation,

$$
\begin{aligned}
-\Delta E &= \int_0^T dt \; \dot{\xi} F_{\text{nc}} \\
&= \int_0^T dt \; \dot{\xi} \left(m\ddot{\xi} + b\dot{\xi} + k\xi - kA_d \cos \omega t - F_c \right),
\end{aligned}
\tag{2.4}
$$

which can be rewritten in terms of multi-harmonic signals as, using Eq. (2.2),

$$\Delta E = \pi k \left(A_d A_1 \cos \theta_1 - \frac{\omega}{Q\omega_0} \sum_{n=1}^{\infty} n^2 A_n^2 \right). \tag{2.5}$$

Note that the dissipation energy is fully expressed by the multi-harmonic responses, with no dependence on the explicit form of F_{nc}. Moreover, the expression can be divided in terms of energy flow, where the positive term represents the external energy influx from the drive and the negative terms the internal dissipation energy. The higher harmonic terms ($n > 1$) reflect the additional internal dissipation due to the higher harmonic motions. Of course, the single

amplitude approximation of Eq. (2.5) reduces well to the previously reported results [5–7].

Now, let us consider F_{nc} having explicit velocity dependence of the form,

$$F_{\text{int}}(z, \dot{z}) = F_c(z) - \Gamma(z)\dot{z}, \tag{2.6}$$

where $\Gamma(z)$ is the friction coefficient [8]. This form is chosen for further investigation as it is one of the most conventional and intuitive representation of the dissipation force [5,8,9]. Inserting Eq. (2.6) to Eq. (2.1), we obtain the following equation of motion for the probe,

$$m\ddot{\xi} + b\dot{\xi} + k\xi = kA_d \cos \omega t + F_c(z + \xi) - \Gamma(z + \xi)\dot{\xi}. \tag{2.7}$$

From this equation, let us proceed to derive two explicit force-reconstruction formulas, corresponding to the two MHAFM operation modes.

2.2.1 Amplitude-Modulation MHAFM.

In amplitude-modulation MHAFM, the cantilever is driven at a constant driving amplitude and frequency, and responses at the driving frequency and its higher harmonics is measured. To proceed, let us assume $|A_1| \gg |A_n|$ for $n > 1$, corresponding to typical MHAFM experimental observations [10–12]. Also, let us approximate $z + \xi_0 \approx z$ in accordance with previous dynamical AFM literatures [5,13], as the mean deflection is negligible with the use of stiff cantilevers. Integrating Eq. (2.7) with the weight functions $\sin(n\omega t + n\theta_1)$ and $\cos(n\omega t + n\theta_1)$

gives,

$$\int_0^\pi \frac{d\tau}{\pi} F_c(z + A_1 \cos \tau) \cos n\tau \ =$$

$$-\delta_{n1} \left(\frac{kA_d}{2} \sin \theta_1 \right) \ + \ \frac{1}{2} \operatorname{Re} \left[\tilde{A}_n \tilde{H}_n^{-1} \right], \tag{2.8}$$

$$\int_0^\pi \frac{d\tau}{\pi} \Gamma(z + A_1 \cos \tau) \sin \tau \sin n\tau \ =$$

$$\delta_{n1} \left(\frac{kA_d}{2A_1\omega} \cos \theta_1 \right) - \frac{1}{2A_1\omega} \ \operatorname{Im} \ \left[\tilde{A}_n \tilde{H}_n^{-1} \right]. \tag{2.9}$$

Here, δ_{n1} is the Kronecker delta, $\tilde{A}_n \equiv A_n e^{i\theta_n}$ and $\tilde{H}_n \equiv H(in\omega)e^{in\theta_1} i^{1-n}$, where $H(i\omega) \equiv (k - m\omega^2 + ib\omega)^{-1}$ is the transfer function of the cantilever. Note that A_n and θ_n are uniquely determined by the above equations for any positive integer n.

The integrals used to express the multi-harmonics can be converted to infinite summations. Let us express the conservative and dissipative forces in terms of the Laplace transformations of functions, $C(\lambda)$ and $\gamma(\lambda)$,

$$F_c(z) \equiv \int_0^\infty d\lambda e^{-\lambda z} C(\lambda), \tag{2.10}$$

$$\Gamma(z) \equiv \int_0^\infty d\lambda e^{-\lambda z} \gamma(\lambda). \tag{2.11}$$

Then, the integrals in Eqs. (8) and (9) can be written as,

$$(-1)^n \int_0^\infty d\lambda C(\lambda) e^{-\lambda z} I_n(\lambda A_1) \ =$$

$$-\delta_{n1} \left(\frac{kA_d}{2} \sin \theta_1 \right) + \frac{1}{2} \ \operatorname{Re} \ \left[\tilde{A}_n \tilde{H}_n^{-1} \right], \tag{2.12}$$

$$(-1)^{n+1} n \int_0^\infty d\lambda \gamma(\lambda) e^{-\lambda z} \frac{I_n(\lambda A_1)}{\lambda A_1} \ =$$

$$\delta_{n1} \left(\frac{kA_d}{2A_1\omega} \cos \theta_1 \right) - \frac{1}{2A_1\omega} \ \operatorname{Im} \ \left[\tilde{A}_n \tilde{H}_n^{-1} \right]. \tag{2.13}$$

18

Here, I_n is the nth-order modified Bessel function of the first kind, which is defined as,

$$I_n\left(\lambda A_1\right) = \sum_{k=0}^{\infty} \frac{\left(\lambda A_1\right)^{2k+n}}{2^{(2k+n)}k!(k+n)!}. \qquad (2.14)$$

Inserting the formula to Eqs. (2.12) and (2.13), we derive the following equations,

$$\sum_{k=0}^{\infty} \frac{A_1^{2k+n}(z)}{2^{(2k+n)}k!(k+n)!} \frac{d^{2k+n}}{dz^{2k+n}} F_c(z) =$$
$$\delta_{n1}\left(-\frac{kA_d}{2}\sin\theta_1(z)\right) + \frac{1}{2} \quad \mathrm{Re}\quad \left[\tilde{A}_n(z)\tilde{H}_n^{-1}(z)\right], \qquad (2.15)$$

$$\sum_{k=0}^{\infty} n\frac{A_1^{2k+n-1}(z)}{2^{(2k+n)}k!(k+n)!} \frac{d^{2k+n-1}}{dz^{2k+n-1}}\Gamma(z) =$$
$$\delta_{n1}\left(\frac{kA_d}{2A_1(z)\omega}\cos\theta_1(z)\right) - \frac{1}{2A_1(z)\omega} \quad \mathrm{Im}\quad \left[\tilde{A}_n(z)\tilde{H}_n^{-1}(z)\right]. \qquad (2.16)$$

Notice that the leading term in the nth harmonic signals is proportional to the nth derivatives of F_c and the $(n-1)$th derivatives of Γ.

2.2.2 Frequency-Modulation MHAFM

In FM-AFM, the driving amplitude and frequency are controlled to ensure fixed oscillation amplitude A_1 at the resonance frequency ω_{res} ($\theta_1 = 0$) by using feedback loops. Thus, frequency-modulation MHAFM measures higher harmonic responses $\tilde{A}_n \equiv A_n e^{i\theta_n}$ with the resonance frequency shift $\Omega(z) \equiv (\omega_{\mathrm{res}}(z) - \omega_0)/\omega_0$ and driving amplitude $A_d(z)$. Using again the assumptions of $|A_1| \gg |A_n|$ for $n > 1$ and $z + \xi_0 \approx z$, we multiply Eq. (2.7) by $\sin(n\omega_0(1+\Omega)t)$ and

19

$\cos(n\omega_0(1+\Omega)t)$, and integrate to derive the equations for $\tilde{A}_n$ as,

$$\int_0^\pi \frac{d\tau}{\pi} F_c(z + A_1 \cos\tau) \cos n\tau = \frac{1}{2} \operatorname{Re}\left[\tilde{A}_n \hat{H}_n^{-1}\right], \qquad (2.17)$$

$$\int_0^\pi \frac{d\tau}{\pi} \Gamma(z + A_1 \cos\tau) \sin\tau \sin n\tau =$$

$$\delta_{n1}\left(\frac{kA_d}{2A_1\omega_0(1+\Omega)}\right) - \frac{1}{2A_1\omega_0(1+\Omega)} \operatorname{Im}\left[\tilde{A}_n \hat{H}_n^{-1}\right]. \tag{2.18}$$

Here, $\hat{H}_n \equiv H(in\omega_0(1+\Omega))i^{1-n}$, not to be confused with $\tilde{H}_n$ in the previous subsection. Solving Eqs. (2.17) and (2.18), we can analytically derive the multi-harmonic response $\tilde{A}_n$ up to an arbitrary order n. Note these expressions are more general than those previously reported [8], as the latter uses the low bandwidth $(Q \gg 1)$ approximation.

Similarly, let us convert the integrals to infinite sum of higher order derivatives using the Laplace transformation as

$$\sum_{k=0}^\infty \frac{A_1^{2k+n}}{2^{(2k+n)}k!(k+n)!} \frac{d^{2k+n}}{dz^{2k+n}} F_c(z) = \frac{1}{2} \operatorname{Re}\left[\tilde{A}_n(z)\hat{H}_n^{-1}(z)\right], \qquad (2.19)$$

$$\sum_{k=0}^\infty n\frac{A_1^{2k+n-1}}{2^{(2k+n)}k!(k+n)!} \frac{d^{2k+n-1}}{dz^{2k+n-1}} \Gamma(z) =$$

$$\delta_{n1}\left(\frac{kA_d(z)}{2A_1\omega_0(1+\Omega(z))}\right) - \frac{1}{2A_1\omega_0(1+\Omega(z))} \operatorname{Im}\left[\tilde{A}_n(z)\hat{H}_n^{-1}(z)\right]. \tag{2.20}$$

Let us make several observations regarding the expressions of the higher harmonics of the cantilever motion. Firstly, for a conservative system without damping, the higher harmonic signals are given explicitly as (see Eq. (2.19)),

$$\tilde{A}_n = 2\hat{H}_n \sum_{k=0}^\infty \frac{A_1^{2k+n}}{2^{(2k+n)}k!(k+n)!} \frac{d^{2k+n}}{dz^{2k+n}} F_c(z), \qquad (2.21)$$

20

where the leading term is proportional to the nth derivative of F_c and the rest is attenuated exponentially. Thus, the higher harmonic signals due to interatomic forces that follow the inverse power laws are more localized close to the surface atoms, which explains the enhanced lateral resolution in MHAFM. Moreover, the expression of the higher harmonics as in Eq. (2.21) implies that the derivative of F_c of order n can be calculated through summation of higher harmonic signals of order n and higher. In other words, complete characterization of F_c is possible through measurement of the multi-harmonic signals, enabling detailed description of the properties of samples. This explains how simultaneous characterization of the local properties have been possible in former works [12, 14–16]. The main difference is that they chose a particular contact model (eg. Derjaguin-Muller-Toporov model of elastic contact) to derive equations connecting the higher harmonics and parameters for the contact model. In contrast, this approach provides a general relation of the higher harmonics and arbitrary interaction, from which we can describe the distance-dependent characteristics of the interaction force.

2.3 Simulation Results

To observe the behaviors of the higher harmonics of DFM probe, let us use the Lennard-Jones (LJ) type force, which is defined as,

$$F_{\mathrm{LJ}}(z) = F_0\left(\frac{l^6}{3z^6} - \frac{l^2}{z^2}\right), \tag{2.22}$$

where $F_0 = 0.9\,\mathrm{nN}$ is a constant and $l = 0.3\,\mathrm{nm}$ is the characteristic length.

For simulation of the multi-harmonic signals, we chose $0.33\,l = 0.1\,\mathrm{nm}$ for the free (fixed) oscillation amplitude in AM-AFM (FM-AFM) because amplitudes comparable to the decay length of the interaction ($0.5\,l = 0.15\,\mathrm{nm}$) are typically used in DFM experiments.

The mechanical parameters of the cantilever were set to values typical in tuning fork-based AFM experiments with $f_0 = 22\,000\,\mathrm{Hz}$, $k_0 = 2\,000\,\mathrm{N\,m^{-1}}$, $Q = 1\,000$ for AM-AFM and $f_0 = 22\,000\,\mathrm{Hz}$, $k_0 = 2\,000\,\mathrm{N\,m^{-1}}$, $Q = 10\,000$ for FM-AFM. We use the spacing of the data points $\Delta z = 1\,\mathrm{pm}$ and the total number of data points $N \approx 5000$.

Let us demonstrate the generation multi-harmonic signals in AM-AFM up to the sixth harmonic with free oscillation amplitude $A_1^{free} = A_1(\infty) = 0.1\,\mathrm{nm}$ (or $0.33\,l$) as shown in Fig. 2.1. The signals are calculated at approximately 5000 data points spaced with $\Delta z = 1\,\mathrm{pm}$ and mechanical parameters of the cantilever as $f_0 = 22\,000\,\mathrm{Hz}$, $k_0 = 2\,000\,\mathrm{N\,m^{-1}}$, $Q = 1\,000$. Interestingly, the amplitude and phase of the higher harmonic signals from $n = 2$ to 6 in Figs. 2.1(b-f) exhibit different behaviors with those at the driving frequency ($n = 1$) given in Fig. 2.1(a). The higher harmonic amplitudes increase sharply due to increased nonlinearity as the force changes more rapidly after $z = z_{\mathrm{inf}} = 0.37\,\mathrm{nm}$, which then decrease since the oscillation range given as $2A_1$ is narrowed, reducing the nonlinear effects on the probe.
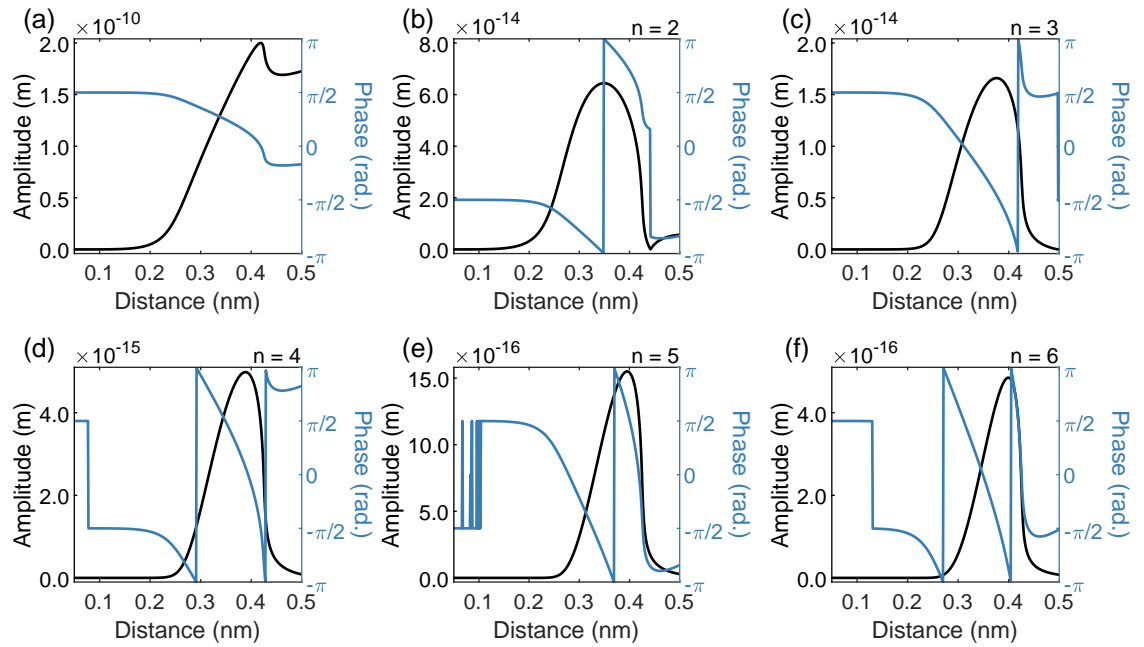
Figure 2.1: Simulated multi-harmonic signals in amplitude-modulation AFM. (a) Amplitude and phase of the signal at the driving frequency. Signals at the higher harmonics of the driving frequency are calculated for (b) second, (c) third, (d) fourth, (e) fifth, and (f) sixth harmonics.

Let us also show multi-harmonic signals in FM-AFM in Fig. 2.2, generated using fixed oscillation amplitude $A_1^{fixed} = A_1 = 0.1\,\text{nm}$ (or $0.33\,l$). Here, the signals are calculated for approximately 5000 data points spaced with $\Delta z = 1\,\text{pm}$ and mechanical parameters of the cantilever as $f_0 = 22\,000\,\text{Hz}$, $k_0 = 2\,000\,\text{N}\,\text{m}^{-1}$, $Q = 10\,000$. The resonance frequency shift and the driving amplitude are shown in Fig. 2.2(a) and the higher harmonics in Figs. 2.2(b-f). Since A_1 is kept constant in FM-AFM, attenuation of the nonlinear effects by the reduction of A_1 is absent, resulting monotonic increase of A_n for $n > 1$. Note that phase information of the higher harmonic signals is not important when the force is conservative, since $\tilde{A}_n$ is purely real for odd n and purely imaginary for even n.
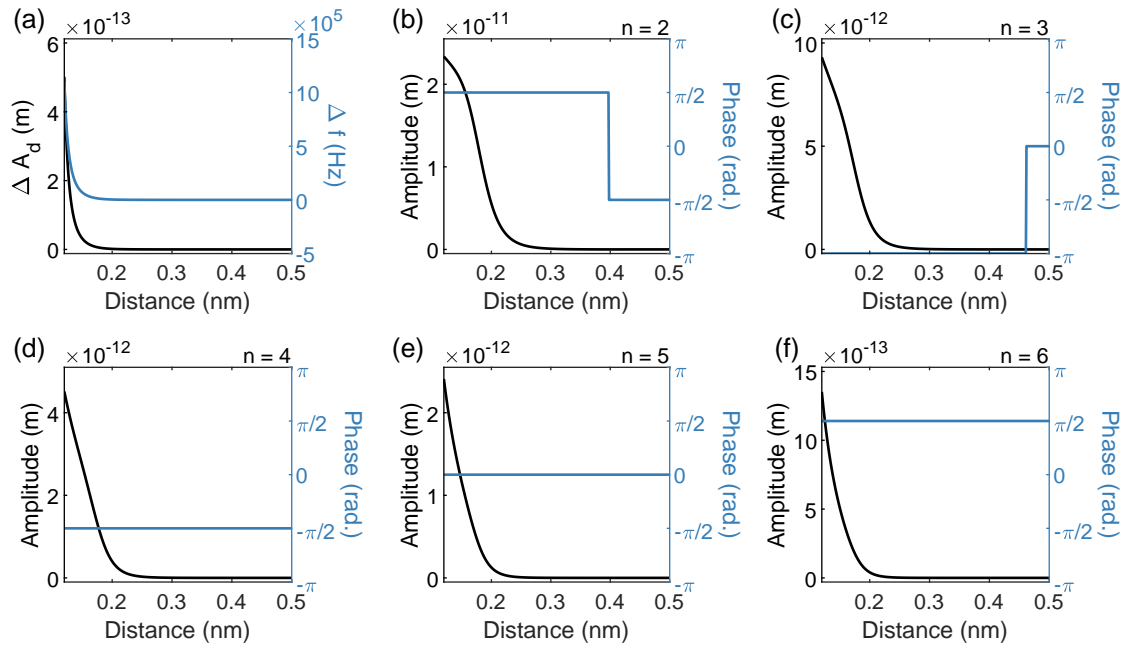
Figure 2.2: Simulated multi-harmonic signals in frequency-modulation AFM. (a) Frequency shift and driving amplitude change. Signals at the higher harmonics of the driving frequency are calculated for (b) second, (c) third, (d) fourth, (e) fifth, and (f) sixth harmonics.

25

2.4 Conclusion

Higher harmonic responses in DFM have been theoretically examined in this chapter. Exact and analytic expressions for the multi-harmonics have been derived for both AM-AFM and FM-AFM in integral and summation representations. Simulation results have demonstrated the behavior of the higher harmonics when the interaction is characterized by the Lennard-Jones type potential. Also, energy dissipation due to tip-sample interaction has been shown to be less than the estimated value in theories based on single-frequency approximations since higher harmonic motions causes additional internal energy loss. This work provides a rigorous theoretical tool for analysis of higher harmonic signals in both AM-AFM and FM-AFM.

Bibliography

[1] Vampa, G. & Villeneuve, D. M. To the extreme. *Nature Physics* **11**, 529–530 (2015).

[2] Ghimire, S. & Reis, D. A. High-harmonic generation from solids. *Nature Physics* **15**, 10–16 (2018).

[3] Lakhotia, H. *et al.* Laser picoscopy of valence electrons in solids. *Nature* **583**, 55–59 (2020).

[4] Sader, J. E. & Jarvis, S. P. Accurate formulas for interaction force and energy in frequency modulation force spectroscopy. *Appl. Phys. Lett.* **84**, 1801–1803 (2004).

[5] Lee, M. & Jhe, W. General theory of amplitude-modulation atomic force microscopy. *Phys. Rev. Lett.* **97**, 036104 (2006).

[6] Anczykowski, B., Gotsmann, B., Fuchs, H., Cleveland, J. P. & Elings, V. B. How to measure energy dissipation in dynamic mode atomic force microscopy. *Appl. Surf. Sci.* **140**, 376–382 (1999).

[7] Giessibl, F. J. Advances in atomic force microscopy. *Rev. Mod. Phys.* **75**, 949–983 (2003).

[8] Dürig, U. Interaction sensing in dynamic force microscopy. *New J. Phys.* **2**, 5–5 (2000).

[9] Dagdeviren, O. E., Zhou, C., Altman, E. I. & Schwarz, U. D. Quantifying tip-sample interactions in vacuum using cantilever-based sensors: An analysis. *Phys. Rev. Appl.* **9**, 044040 (2018).

[10] Stark, R. W. & Heckl, W. M. Higher harmonics imaging in tapping-mode atomic-force microscopy. *Rev. Sci. Instrum.* **74**, 5111–5114 (2003).

[11] Giessibl, F. J. Higher-harmonic atomic force microscopy. *Surf. Interface Anal.* **38**, 1696–1701 (2006).

[12] Raman, A. *et al.* Mapping nanomechanical properties of live cells using multi-harmonic atomic force microscopy. *Nat. Nanotechnol.* **6**, 809–814 (2011).

[13] Garcia, R. & Pérez, R. Dynamic atomic force microscopy methods. *Surf. Sci. Rep.* **47**, 197–301 (2002).

[14] Gramazio, F. *et al.* Functional dependence of resonant harmonics on nanomechanical parameters in dynamic mode atomic force microscopy. *Beilstein J. Nanotechnol.* **8**, 883–891 (2017).

[15] Gramazio, F., Lorenzoni, M., Perez-Murano, F., Evangelio, L. & Fraxedas, J. Quantification of nanomechanical properties of surfaces by higher harmonic monitoring in amplitude modulated afm imaging. *Ultramicroscopy* **187**, 20–25 (2018).

[16] Shaik, N. H., Reifenberger, R. G. & Raman, A. Nanomechanical mapping in air or vacuum using multi-harmonic signals in tapping mode atomic force microscopy. *Nanotechnology* **31**, 455502 (2020).

Chapter 3

Force Reconstruction in Dynamic Force Microscopy using Multi-harmonic Signal Analysis

3.1 Introduction

Measuring interaction forces using dynamic force microscopy (DFM) requires reconstruction procedure from the measured signals, which is called force reconstruction. Force reconstruction in DFM is a mathematically nontrivial task since the motion of the DFM probe is determined not by a constant force, but rather by a varying force with respect to the range the probe oscillates.

This chapter develops a universal multi-harmonic atomic force microscopy (MHAFM) platform for exact, robust and efficient force reconstruction. First,

from analytical formulas for higher harmonic responses in DFM, explicit reconstruction formulas for conservative and dissipative forces are derived, valid for all oscillation amplitudes and entire tip-sample distances. Analytic expressions of these formulas are derived separately for each operation mode of DFM. The chapter goes on to demonstrate the exactness of the formulas by performing force reconstruction for the Lennard-Jones type force model, and find that the approximate reconstruction results, obtained by including only a finite number of harmonics, show superior accuracy over the Sader-Jarvis (SJ) method. Finally, the robustness of the MHAFM force reconstruction scheme against the oscillation-amplitude error is demonstrated using the Stillinger-Weber type force model, which clearly shows that MHAFM platform remarkably overcomes the force-inversion instability inherent in the conventional methods.

3.2   Theoretical Formulation

3.2.1   Amplitude-Modulation MHAFM

The multi-harmonic responses for amplitude-modulation MHAFM is derived in the previous chapter as

$$
\int_0^\pi \frac{d\tau}{\pi} F_c(z + A_1 \cos\tau) \cos n\tau \; = \\
-\delta_{n1} \left(\frac{k A_d}{2} \sin\theta_1 \right) \; + \; \frac{1}{2} \text{Re} \left[\tilde{A}_n \tilde{H}_n^{-1} \right],
\qquad (3.1)
$$

$$\int_0^\pi \frac{d\tau}{\pi} \Gamma\left(z + A_1 \cos \tau\right) \sin \tau \sin n\tau \quad =$$

$$\delta_{n1} \left(\frac{kA_d}{2A_1\omega} \cos \theta_1\right) - \frac{1}{2A_1\omega} \quad \text{Im} \quad \left[\tilde{A}_n \tilde{H}_n^{-1}\right], \tag{3.2}$$

where δ_{n1} is the Kronecker delta, $\tilde{A}_n \equiv A_n e^{i\theta_n}$ and $\tilde{H}_n \equiv H(in\omega)e^{in\theta_1}i^{1-n}$, where $H(i\omega) \equiv (k - m\omega^2 + ib\omega)^{-1}$ is the transfer function of the cantilever. The equivalent expressions are as the following:

$$\sum_{k=0}^\infty \frac{A_1^{2k+n}(z)}{2^{(2k+n)}k!(k+n)!} \frac{d^{2k+n}}{dz^{2k+n}} F_c(z) \quad =$$

$$\delta_{n1} \left(-\frac{kA_d}{2} \sin \theta_1(z)\right) + \frac{1}{2} \quad \text{Re} \quad \left[\tilde{A}_n(z)\tilde{H}_n^{-1}(z)\right], \tag{3.3}$$

$$\sum_{k=0}^\infty n\frac{A_1^{2k+n-1}(z)}{2^{(2k+n)}k!(k+n)!} \frac{d^{2k+n-1}}{dz^{2k+n-1}} \Gamma(z) \quad =$$

$$\delta_{n1} \left(\frac{kA_d}{2A_1(z)\omega} \cos \theta_1(z)\right) - \frac{1}{2A_1(z)\omega} \quad \text{Im} \quad \left[\tilde{A}_n(z)\tilde{H}_n^{-1}(z)\right]. \tag{3.4}$$

Next, consider the following relation,

$$\sum_{n=0}^m \begin{pmatrix} 2m + 1 \\ m - n \end{pmatrix} (2n + 1)(-1)^n = 0 \qquad \text{for } m > 0, \tag{3.5}$$

to eliminate the infinite sum of the higher-order derivatives of force, and derive the *exact* expressions of dF_c/dz and Γ using the multi-harmonic signals,

$$\frac{d}{dz}F_c(z) \quad = \quad -\frac{kA_d}{A_1(z)} \sin \theta_1(z)$$

$$- \quad \sum_{m=1}^\infty \frac{(-1)^m(2m - 1)}{A_1(z)} \text{Re}\left[\tilde{A}_{2m-1}(z)\tilde{H}_{2m-1}^{-1}(z)\right], \tag{3.6}$$

$$\Gamma(z) \quad = \quad \frac{kA_d}{A_1(z)\omega} \cos \theta_1(z)$$

$$+ \quad \sum_{m=1}^\infty \frac{(-1)^m}{A_1(z)\omega} \text{Im}\left[\tilde{A}_{2m-1}(z)\tilde{H}_{2m-1}^{-1}(z)\right]. \tag{3.7}$$

32

Integration of Eq. (3.6) gives us the following.

$$
\begin{aligned}
F_c(z) &= \int_z^\infty dz' \left\{ \frac{kA_d}{A_1(z')} \sin\theta_1(z') \right. \\
&+ \left. \sum_{m=1}^\infty \frac{(-1)^m(2m-1)}{A_1(z')} \operatorname{Re}\left[\tilde{A}_{2m-1}(z') \tilde{H}_{2m-1}^{-1}(z') \right] \right\}.
\end{aligned}
\tag{3.8}
$$

3.2.2 Frequency-Modulation MHAFM

Force reconstruction formulas for frequency-modulation MHAFM is similarly derived from the analytical expressions of the multi-harmonic signals, given as

$$
\int_0^\pi \frac{d\tau}{\pi} F_c(z + A_1\cos\tau)\cos n\tau = \frac{1}{2}\operatorname{Re}\left[\tilde{A}_n\hat{H}_n^{-1}\right],
\tag{3.9}
$$

$$
\int_0^\pi \frac{d\tau}{\pi} \Gamma(z + A_1\cos\tau)\sin\tau\sin n\tau =
$$
$$
\delta_{n1}\left(\frac{kA_d}{2A_1\omega_0(1+\Omega)}\right) - \frac{1}{2A_1\omega_0(1+\Omega)} \operatorname{Im}\left[\tilde{A}_n\hat{H}_n^{-1}\right],
\tag{3.10}
$$

where $\hat{H}_n \equiv H(in\omega_0(1+\Omega))i^{1-n}$, different from $\tilde{H}_n$ in the previous subsection. These expressions can equivalently be written using infinite summations as

$$
\sum_{k=0}^\infty \frac{A_1^{2k+n}}{2^{(2k+n)}k!(k+n)!}\frac{d^{2k+n}}{dz^{2k+n}}F_c(z) = \frac{1}{2}\operatorname{Re}\left[\tilde{A}_n(z)\hat{H}_n^{-1}(z)\right],
\tag{3.11}
$$

$$
\sum_{k=0}^\infty n\frac{A_1^{2k+n-1}}{2^{(2k+n)}k!(k+n)!}\frac{d^{2k+n-1}}{dz^{2k+n-1}}\Gamma(z) =
$$
$$
\delta_{n1}\left(\frac{kA_d(z)}{2A_1\omega_0(1+\Omega(z))}\right) - \frac{1}{2A_1\omega_0(1+\Omega(z))} \operatorname{Im}\left[\tilde{A}_n(z)\hat{H}_n^{-1}(z)\right]. \tag{3.12}
$$

The *exact* inversion formulas for the conservative and dissipative forces

are similarly derived as the amplitude-modulation counterparts,

$$F_c(z) = \sum_{m=1}^{\infty} \left\{ (-1)^m (2m-1) \right.$$
$$\left. \times \int_z^{\infty} \frac{dz'}{A_1} \operatorname{Re}\left[\tilde{A}_{2m-1}(z') \hat{H}_{2m-1}^{-1}(z') \right] \right\}, \quad (3.13)$$

$$\Gamma(z) = \frac{kA_d(z)}{A_1\omega_0(1+\Omega(z))}$$
$$+ \sum_{m=1}^{\infty} \frac{(-1)^m}{A_1\omega_0(1+\Omega(z))} \operatorname{Im}\left[\tilde{A}_{2m-1}(z)\hat{H}_{2m-1}^{-1}(z) \right]. \quad (3.14)$$

Let us make several remarks on the reconstruction formulas. First, the reconstruction formulas for both conservative and dissipative forces require $\tilde{A}_n$'s of odd n. For the conservative part, the key to understanding this is that the exact value of dF_c/dz is integrated to derive F_c. In Eq. (3.3), the odd(even)-order derivatives of F_c are linear combinations of the odd (even) harmonics (and vice versa), which explains why dF_c/dz and consequently its integral F_c is a function of odd harmonics. Second, F_c can be efficiently calculated through approximation using a finite upper bound M in the summations in Eqs. (3.8) and (3.13), with M corresponding to the order of approximation. Then, the calculations reduce to M integrations that each require $(O(N))$ computation time, where N is the number of discrete data points. The resulting computation time of this scheme is $(O(MN))$, dramatically faster than both the SJ method [1] that requires integrations for each point $(O(N^2))$, and the matrix method [2] that involves inversion of $N \times N$ matrices $(O(N^k)$ with $2.373 \leq k \leq 3$ depending on the algorithm used). Lastly, while single mode oscillation of the

34

cantilever is assumed in the derivations, the analogous reconstruction formulas can also be derived assuming multiple eigenmodes where one of its resonance frequencies is an exact multiple of ω_{res}, enhancing the corresponding higher harmonic responses [3]. For this, simply replace $H(i\omega)$, used to define $\tilde{H}_n$ and $\hat{H}_n$ respectively in Eqs. (3.7-3.8) and Eqs. (3.13-3.14), by the transfer function of the corresponding eigenmode.

3.3 Reconstruction Results

Let us verify that the reconstruction formulas are exact for the entire range of oscillation amplitudes and tip-sample separations. First, multi-harmonic signals $\tilde{A}_n$ are generated with respect to the model force for both AM-AFM and FM-AFM using Eqs. (3.1-3.2) and (3.9-3.10), respectively. The Lennard-Jones (LJ) type force is chosen for current analysis, which is defined as,

$$F_{\text{LJ}}(z) = F_0 \left(\frac{l^6}{3z^6} - \frac{l^2}{z^2} \right), \tag{3.15}$$

where $F_0 = 0.9\,\text{nN}$ is a constant and $l = 0.3\,\text{nm}$ is the characteristic length. The LJ type force has the inflection point $z_{\text{inf}} = 1.24\,l$ where the curvature of the force changes sign, force-minimum point $z_{\text{f\_min}} = l$, and potential-minimum point $z_{\text{p\_min}} = 0.76\,l$. The oscillation amplitudes are chosen by invoking the inflection point test of Sader *et al.* [4], which gives the amplitude range where single frequency-based conventional force reconstruction methods are unreliable:

$$\sqrt{-\frac{F'_{\text{int}}(z_{\text{inf}})}{F'''_{\text{int}}(z_{\text{inf}})}} \leq A_1 \leq \frac{z_{\text{inf}}}{2}. \tag{3.16}$$

For the LJ type force, the corresponding amplitude range is $0.22\,l < A_1 < 0.62\,l$, which is comparable to λ of the attractive force $(0.5\,l)$. For comprehensive analysis, we use amplitudes that are small $(0.1\,l = 0.03\,\text{nm})$, intermediate $(0.33\,l = 0.1\,\text{nm})$, and large $(0.66\,l = 0.2\,\text{nm})$ with respect to Eq. (3.16), for the free (fixed) oscillation amplitude in AM-AFM (FM-AFM) to generate the multi-harmonic signals.

The mechanical parameters of the cantilever were set to values typical in tuning fork-based DFM experiments with $f_0 = 22\,000\,\text{Hz}$, $k_0 = 2\,000\,\text{N}\,\text{m}^{-1}$, $Q = 1\,000$ for AM-AFM and $f_0 = 22\,000\,\text{Hz}$, $k_0 = 2\,000\,\text{N}\,\text{m}^{-1}$, $Q = 10\,000$ for FM-AFM. The spacing of the data points $\Delta z = 1\,\text{pm}$ and the total number of data points $N \approx 5000$ are chosen accordingly.

Reconstruction results of the interaction forces from the generated AM-AFM and FM-AFM multi-harmonic signals are shown in Figs. 3.1 and 3.2, using an order M approximation of the formulas (Eqs. (3.8) and (3.13)) with varying M. Increasing M leads to more accurate reconstruction results in Figs. 3.1(a-c) and 3.2(a-c) as well as less errors at $z_{\text{p\_min}}$, $z_{\text{f\_min}}$, and z_{inf} in Figs. 3.1(d-f) and 3.2(d-f), demonstrating the exactness of the reconstruction formulas. Futhermore, since the accuracy of the approximation is compromised by the magnitude of the higher harmonics of order $> 2M - 1$, smaller amplitudes result in more accurate reconstructions even at smaller M. For example, the reconstruction errors for AM-AFM at $z_{\text{f\_min}}$ in Figs. 3.1(d-f) are given as 0.02%, 0.3%, and 0.02% using $M = 2$ (small amplitude), 3 (intermediate amplitude), and 6 (large amplitude), respectively. For FM-AFM, the reconstruction errors

at $z_{\text{f\_min}}$ in Figs. 3.2(d-f) are given as 0.03%, 0.8%, and 0.25% using the same M values for each amplitude, except for large amplitude ($M = 9$). These results clearly show superior accuracy over the SJ method by an order of magnitude for intermediate and large amplitudes, and by two orders of magnitude for smaller amplitudes. Additionally, our approach displays superior computational efficiency, with at least ten-fold decrease in the computation time compared to the SJ method as shown in Tabs. 3.1-3.6.
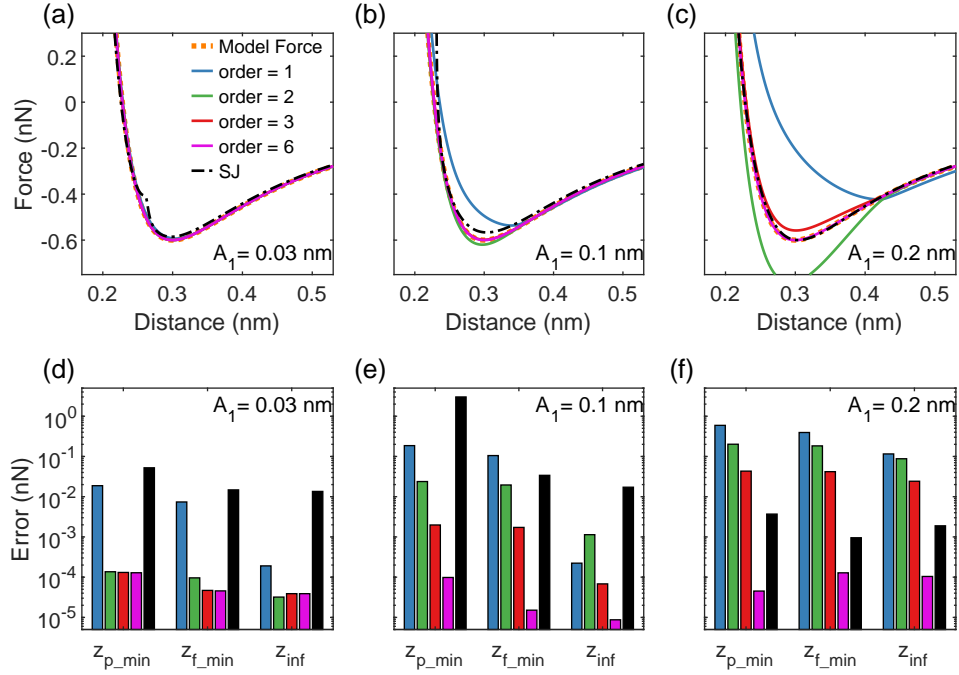
Figure 3.1: Analysis of the reconstructed force in AM-AFM for different free oscillation amplitude A_1. (a-c) Reconstructed force-distance curves using different orders of approximation and those of the Sader-Jarvis method (black) are presented and compared to the model force F_{LJ} (orange). (d-f) Reconstruction errors are calculated for each plot at the potential minimum $z_{\mathrm{p\_min}}$, force minimum $z_{\mathrm{f\_min}}$, and inflection point z_{inf} of F_{LJ}. As shown, increasing the order of approximation reduces the overall error observed at the specific points.
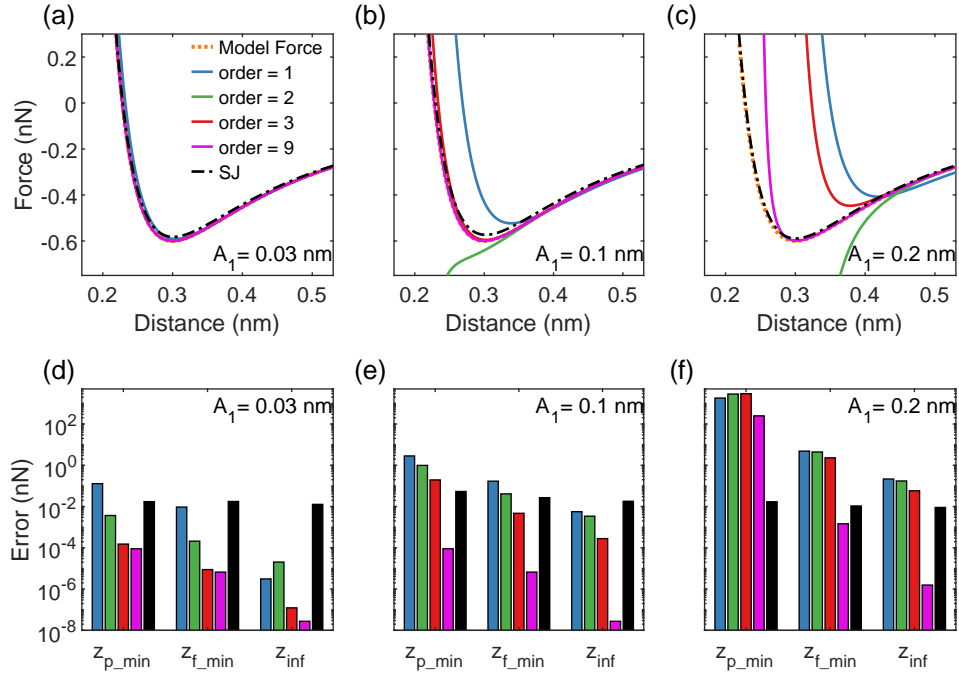
Figure 3.2: Force reconstruction in FM-AFM using different fixed oscillation amplitude A_1. (a-c) Reconstructed force-distance curves of the model force F_{LJ} (orange) using different orders of approximation of the reconstruction formulas. (d-f) Reconstruction errors calculated at z_{p_min}, z_{f_min}, and z_{inf}. The results of the Sader-Jarvis method (black) are also shown for comparison. Similar to the results in AM-AFM, the reconstruction accuracy at such points increases when using higher orders of approximation, reflecting the exactness of the reconstruction formulas.

Method	Error($z = z_{\text{p\_min}}$) (nN)	Error($z = z_{\text{f\_min}}$) (nN)	Error($z = z_{\text{inf}}$) (nN)	Computation time (s)
order = 1	0.01877	0.007394	0.0001907	0.0013
order = 2	0.0001363	9.605e-05	3.199e-05	0.0023
order = 3	0.000131	4.686e-05	3.891e-05	0.0034
order = 6	0.0001287	4.557e-05	3.888e-05	0.0101
Sader-Jarvis	0.05225	0.01476	0.01353	1.497

Table 3.1: Reconstruction results in AM-AFM for small amplitude. The force-reconstruction errors (nN) at the points of interest and the computation times (s) are shown for each reconstruction method.

Method	Error($z = z_{\text{p\_min}}$) (nN)	Error($z = z_{\text{f\_min}}$) (nN)	Error($z = z_{\text{inf}}$) (nN)	Computation time (s)
order = 1	0.186	0.1052	0.0002228	0.0011
order = 2	0.02381	0.01955	0.001138	0.0023
order = 3	0.001981	0.001724	6.805e-05	0.0035
order = 6	9.828e-05	1.513e-05	8.715e-06	0.0061
Sader-Jarvis	3.014	0.03397	0.01722	1.278

Table 3.2: Reconstruction results in AM-AFM for intermediate amplitude. The force-reconstruction errors (nN) at the points of interest and the computation times (s) are shown for each reconstruction method.

Method	Error($z = z_{\text{p\_min}}$) (nN)	Error($z = z_{\text{f\_min}}$) (nN)	Error($z = z_{\text{inf}}$) (nN)	Computation time (s)
order = 1	0.5931	0.3941	0.1155	0.0020
order = 2	0.2014	0.1833	0.08773	0.0037
order = 3	0.04319	0.0419	0.02422	0.0049
order = 6	4.515e-05	0.0001282	0.0001042	0.0105
Sader-Jarvis	0.003696	0.0009537	0.001888	1.340

Table 3.3: Reconstruction results in AM-AFM for large amplitude. The force-reconstruction errors (nN) at the points of interest and the computation times (s) are shown for each reconstruction method.

Method	Error($z = z_{\text{p\_min}}$) (nN)	Error($z = z_{\text{f\_min}}$) (nN)	Error($z = z_{\text{inf}}$) (nN)	Computation time (s)
order $= 1$	0.1287	0.009435	3.104e-06	0.0022
order $= 2$	0.00368	0.00021	2.038e-05	0.0080
order $= 3$	0.0001517	8.825e-06	1.232e-07	0.0096
order $= 9$	8.983e-05	6.667e-06	2.757e-08	0.0236
Sader-Jarvis	0.01731	0.01767	0.01277	0.3956

Table 3.4: Reconstruction results in FM-AFM for small amplitude. The force-reconstruction errors (nN) at the points of interest and the computation times (s) are shown for each reconstruction method.

Method	Error($z = z_{\text{p\_min}}$) (nN)	Error($z = z_{\text{f\_min}}$) (nN)	Error($z = z_{\text{inf}}$) (nN)	Computation time (s)
order $= 1$	2.835	0.1695	0.005641	7.425e-04
order $= 2$	0.9858	0.04106	0.003418	0.0021
order $= 3$	0.195	0.004708	0.0002799	0.0044
order $= 9$	9.015e-05	6.667e-06	2.757e-08	0.0121
Sader-Jarvis	0.05382	0.02686	0.01809	0.3753

Table 3.5: Reconstruction results in FM-AFM for intermediate amplitude. The force-reconstruction errors (nN) at the points of interest and the computation times (s) are shown for each reconstruction method.

Method	Error($z = z_{\text{p\_min}}$) (nN)	Error($z = z_{\text{f\_min}}$) (nN)	Error($z = z_{\text{inf}}$) (nN)	Computation time (s)
order $= 1$	1811	4.851	0.2157	0.0034
order $= 2$	2835	4.405	0.1734	0.0046
order $= 3$	2953	2.293	0.0579	0.0056
order $= 9$	248.8	0.001459	1.568e-06	0.0133
Sader-Jarvis	0.01709	0.01068	0.009035	0.3898

Table 3.6: Reconstruction results in FM-AFM for large amplitude. The force-reconstruction errors (nN) at the points of interest and the computation times (s) are shown for each reconstruction method.

Let us now discuss the robustness of the reconstruction formulas. The resolving power of DFM between two distinct interatomic force laws depends on how precisely the forces can be recovered, which is, in FM-AFM, compromised by the instability of the oscillation amplitude. Although feedback is used to maintain a constant amplitude, the non-conservative tip-sample interaction can lead to variations in the amplitude during the gradual approach of the cantilever, causing spurious reconstruction results. This is expected to be maximized in single frequency-based reconstruction procedures when the amplitude is in the intermediate range (Eq. (3.16)) and when the force has points not infinitely differentiable with respect to z [4], due to greater anharmonic motion of the cantilever within the regime where the force changes rapidly.

To verify the robustness with respect to the amplitude instability, force reconstruction is performed using the *set* oscillation amplitudes $A_{1,\text{set}}$ having $\pm 5\%$ error with respect to the *actual* oscillation amplitude $A_{1,\text{actual}}$ [4].The Stillinger-Weber (SW) type, which approximates the forces between two silicon atoms, serves as a good model force because it changes rapidly at $z \approx 350\,\text{pm}$. The multi-harmonic signals are generated with $A_{1,\text{actual}} = 50\,\text{pm}$, which lies in the range of Eq. (3.16), and the same parameters used for the LJ force. Then, the forces are recovered using $A_{1,\text{set}} = 50\,\text{pm}$ (0% error), 52.5 pm (+5% error), 47.5 pm (-5% error), as shown in Figs. 3.3(a) and 3.3(b). The forces reconstructed with the SJ method show the greatest variance at the force minimum with respect to the amplitude error, whereas it is hardly noticed in the reconstruction using $M = 3$. In addition, the above reconstruction procedures are

repeated using the model force rescaled by different scaling factors; we use 0.9, 0.95, 0.98, 1, 1.02, 1.05, and 1.1, to observe the resolving power of the formulas. Quantitative analysis of the force minimum of the reconstruction results in Figs. 3.3(c) and 3.3(d) reveals that multi-harmonic consideration allows to resolve the rescaled SW type forces at $\approx 2\%$ precision, which is a five-fold improvement over the SJ method.
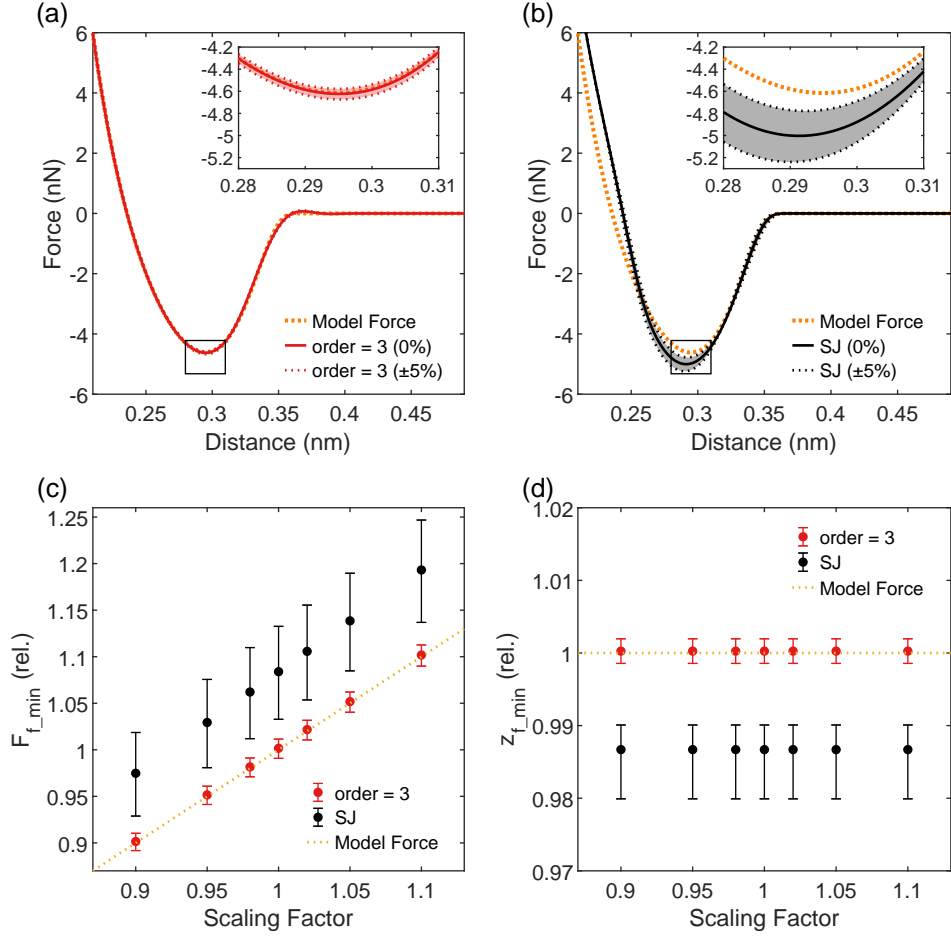
Figure 3.3: Robustness of force reconstruction with respect to amplitude error. (a-b) Reconstructed forces from the signals generated using the SW type force (orange) and fixed oscillation amplitude $A_{1,\text{actual}} = 50\,\text{pm}$, assuming no error (0% error, solid line) and $\pm 5\%$ error (dotted line) with respect to $A_{1,\text{actual}}$. Different scaling factors are used to rescale the SW type force, where the force minimum of the reconstruction results are evaluated in terms of (c) relative force and (d) relative distance with respect to the original SW type force minimum. The error bars delimit the relative position of the force minimum assuming $\pm 5\%$ amplitude error.

3.4 Conclusion

The universal theory of DFM based on multi-harmonic signal analysis is derived in this chapter. This method enables exact and robust reconstruction of the conservative and dissipative forces in both amplitude- and frequency-modulation AFM, regardless of the oscillation amplitudes and tip-sample distances. Even when approximated reconstruction formulas are used, higher accuracy over the SJ method with less computation time is found. Force reconstruction using the multi-harmonic signal analysis is also demonstrated to be robust with respect to the oscillation amplitude error, overcoming the intrinsic reconstruction instability of the conventional methods. The results demonstrate versatility and efficiency for accurate and precise force measurements beyond the limits of conventional DFM.

Bibliography

[1] Sader, J. E. & Jarvis, S. P. Accurate formulas for interaction force and energy in frequency modulation force spectroscopy. *Appl. Phys. Lett.* **84**, 1801–1803 (2004).

[2] Giessibl, F. J. A direct method to calculate tip–sample forces from frequency shifts in frequency-modulation atomic force microscopy. *Appl. Phys. Lett.* **78**, 123–125 (2001).

[3] Sahin, O., Quate, C. F., Solgaard, O. & Atalar, A. Resonant harmonic response in tapping-mode atomic force microscopy. *Phys. Rev. B* **69**, 165416 (2004).

[4] Sader, J. E., Hughes, B. D., Huber, F. & Giessibl, F. J. Interatomic force laws that evade dynamic measurement. *Nat. Nanotechnol.* **13**, 1088–1091 (2018).

Chapter 4

Conclusion

Dynamic force microscopy (DFM) is a powerful tool in surface science that realized characterization of structures and quantification of forces at the atomic and molecular scale. Yet, force reconstruction, which is the inversion process from the DFM probe oscillations to force-distance curves, becomes an ill-posed problem when the oscillation amplitude becomes comparable to the decay length of the interaction λ. The ill-posed behavior is caused by the anharmonic motions of the probe, which undermine the accuracy and stability of the single frequency based reconstruction methods. Hence, multi-harmonic signal analysis can be applied to measure the motion of the probe not only at its resonance, but also at its higher harmonics, since the higher harmonics possess information pertaining to the nonlinearities of tip-sample interactions.

DFM using multi-harmonic signal analysis has been formulated in this thesis through the following steps. First, higher harmonic motions of the DFM

probe have been studied. Exact and analytic expressions for the higher harmonics has been derived in both amplitude-modulation (AM-AFM) and frequency-modulation atomic force microscopy (FM-AFM) for arbitrary conservative and dissipative forces. It has been shown that higher harmonics are more localized to the surface such that measuring higher harmonics can lead to enhanced resolution imaging. Next, a novel force reconstruction method using multi-harmonic signals has been conceived. This approach allows universal reconstruction of conservative and dissipative force in AM-AFM and FM-AFM for all oscillation amplitudes and entire tip-sample distance. The approximated form of the reconstruction formula, which uses only the first few harmonics, has been shown to yield at least ten-fold increase in accuracy and five-fold increase in precision compared to the most widely used SJ method. Also, the reconstruction formulas are mathematically simple, resulting at least ten-fold decrease in computation time compared to the SJ method.

This thesis extends the existing power of DFM in condensed matter physics. Enhanced resolution imaging of material surface using higher harmonic analysis can reveal hidden physicochemical features of materials. Accurate force measurements using the reconstruction formulas can allow resolving molecules of similar configurations and identifying new types of inter-atomic interactions. Great potential impacts on characterization of electronic properties are expected as well, as DFM can be implemented in scanning tunnelling microscopy or conductive AFM.

초　　록

동역학 힘 현미경은 물질 표면의 구조와 특성을 원자 및 분자 단위에서 측정하는 도구로써 응집물질 물리뿐 아니라 화학, 생물학, 재료공학 등 다양한 학문의 발전에 이바지하였다. 이러한 업적이 가능했던 이유는 동역학 힘 현미경이 마이크로미터부터 나노미터 이하의 분해능으로 국소적인 영역에서 탐침과 시료 사이에 상호작용하는 물리적인 힘을 측정할 수 있기 때문이다. 동역학 힘 현미경에서의 힘 측정은 시료와의 상호작용으로 인해 섭동된 탐침의 움직임으로부터 힘을 역산하는 힘 복원이라는 과정을 거쳐야 한다. 하지만 가장 상용되는 힘 복원 방법론은 탐침의 진동 진폭이 상호작용의 감쇠길이와 상응하게 되면 정확도가 떨어지고 복원식이 불안정해진다는 문제점이 제기되었다. 해당 진폭에서 이러한 문제점이 생기는 이유는 기존의 방법론들의 탐침의 움직임이 단순 조화 진동을 하고 있다는 가정이 힘이 급격하게 변하는 구간에서 고조파 진동이 상당해짐에 따라 깨지게 되기 때문이다. 결과적으로 모든 진폭과 탐침-시료 거리에서 유효한 일반적인 힘 복원 방법론의 필요성이 대두되었다.

이 논문에서는 다중 조파 신호 분석을 이용한 동역학 힘 현미경법을 이러한 문제점의 해결책으로 제시한다. 이 새로운 플랫폼은 보편적인 조건에서 동역학 힘 현미경의 탐침의 공명 진동수 신호뿐 아니라 고조파 진동수 신호를 고려하여 힘 복원을 한다. 이 논문은 다음 단계들을 거쳐 다중 조파 신호 기반 현미경법을 구축한다. 우선, 동역학 힘 현미경에서 나타나는 고조파 신호를 이론적으로 탐구한다. 동역학 힘 현미경의 두 가지 작동방식인 진폭 변조와 주파수 변조에서 임의의 보존력과 비보존력을 가정할 때 생성되는 고조파 신호의 정확하고 해석

적인 표현식을 구한다. 그다음으로 동역학 힘 현미경의 두 가지 작동방식을 위한 일반적인 힘 복원 방법론을 제시한다. 이 방법론은 모든 진동 진폭과 탐침-시료 거리에 대해 정확하게 힘을 복원한다. 이러한 접근 방식은 기존의 방법론에 비해 두 가지 측면에서 월등히 뛰어나다: (i) 복원식들의 근사식을 사용하더라도 더 높은 정확도와 계산속도로 힘을 복원하며 (ii) 진폭 오류에 대해 더 강인하여 기존 방법론의 힘 복원 불안정성을 극복한다. 이 연구가 향후 다방면의 동역학 힘 현미경 실험에 접목되어 단분자 검출, 원자 단위의 물리-화학적 힘 규명, 새로운 전자 전달 성질 발견 등에 응용될 것을 기대한다.

주요어 : 동역학 힘 현미경, 원자 힘 현미경, 다중조파 원자 힘 현미경, 주파수 분석, 조파 분석, 비선형 동역학

학 번 :   2019-22272